Materialia 15 (2021) 100997

Contents lists available at ScienceDirect

Materialia

journal homepage: www.elsevier.com/locate/mtla

# Synergistic alloy design concept for new high-strength Al–Mg–Si thick plate alloys

Florian Schmid[a,*], Irmgard Weißensteiner[a], Matheus A. Tunes[b], Thomas Kremmer[b], Thomas Ebner[c], Roland Morak[c], Peter J. Uggowitzer[b], Stefan Pogatscher[a,*]

[a] Christian Doppler Laboratory for Advanced Aluminum Alloys, Chair of Nonferrous Metallurgy, Montanuniversitaet Leoben, Franz-Josef Strasse 18, 8700 Leoben, Austria
[b] Chair of Nonferrous Metallurgy, Montanuniversitaet Leoben, Franz-Josef Strasse 18, 8700 Leoben, Austria
[c] AMAG rolling GmbH, Lamprechtshausener Strasse 61, Postfach 32, 5282 Ranshofen, Austria

ARTICLE INFO

*Keywords:*
Aluminum alloys
Precipitation strengthening
Alloy design
Wrought alloys

ABSTRACT

With the aim of fully exploiting the advantageous strength-to-weight ratio evident in Al–Mg–Si alloys, this study presents measures for increasing the yield strength of an EN AW-6082 type plate alloy. In addition to describing the thermodynamic simulation-based adjustment of age-hardenable elements (Si, Mg and Cu) and a modified artificial ageing treatment, it investigates the effects of adding a small amount of Zr. The significant strengthening induced by adding Zr is correlated with sub-grain boundary hardening in a recovered microstructure after solution annealing at 570 °C, compared with the almost entirely recrystallized microstructure in an unmodified EN AW-6082 alloy. In combination with a maximum dissolvable number of age-hardenable elements and interrupted quenching, which comprises an improved heat treatment strategy for thick plates, it is seen that the yield strength can be increased by more than 40% to 411 MPa compared to conventional EN AW-6082 base material as verified by tensile testing. In the study scanning electron microscopy and scanning transmission electron microscopy were performed for microstructural characterization with a focus on particle and deformation analysis. All individual contributions which generated the superior strength are calculated and discussed in order to reveal the microstructure-property relationship.

## 1. Introduction

Weight-optimized design has become a top priority in the transport sector because it facilitates substantial $CO_2$ reduction [1]. Low-density Al alloys, especially age-hardenable Al–Mg–Si (6xxx) plate alloys, are currently a preferred choice. In addition to their medium to high strength, thick plates made from 6xxx-alloys combine high fracture toughness, good corrosion resistance and weldability. They also feature good recyclability at a moderate price. To further exploit the potential of these alloys and promote their selection, an increase of their strength-to-weight ratio to more favorable levels seems to broaden their field of applications [2–4].

Work hardening plays a key role in sheet materials. Deformation-induced structures such as dislocations and cell structures which originate from cold rolling contribute significantly to enhanced strength values in thin semi-finished products [2]. However, plate alloys, which are deformed at high temperatures only, do not necessarily experience strengthening from this processing step because their increased dislocation density wanes due to recovery processes [5]. In addition, the solution annealing treatment for Al–Mg–Si alloys is typically performed above 530 °C, which weakens hardening via cold working [6]. Several other hardening mechanisms are also active in thick plates, of which strengthening via the formation of metastable Mg and Si containing $\beta$''-phases upon artificial aging is the most important [2,7]. Adding Cu enhances the strength response further, mainly due to the occurrence of L- and Q'-phases [8,9]. Incorporation of Cu into hardening phases which contain Mg and Si also takes place. All of these alloying elements may also contribute distinctly to solid solution hardening [10].

In the course of industrial heat treatment, high strength Al–Mg–Si alloys with a Mg and Si solute content exceeding 1% suffer from a loss of age hardening potential which is caused by natural aging (NA) during room temperature (RT) storage between solution annealing and artificial aging [11,12]. Natural aging in plates may be suppressed by applying interrupted quenching (IQ) to an elevated temperature and

* Corresponding authors.
*E-mail addresses:* florian.schmid@unileoben.ac.at (F. Schmid), irmgard.weissensteiner@unileoben.ac.at (I. Weißensteiner), matheus.tunes@unileoben.ac.at (M.A. Tunes), thomas.kremmer@unileoben.ac.at (T. Kremmer), thomas.ebner@amag.at (T. Ebner), roland.morak@amag.at (R. Morak), peter.uggowitzer@unileoben.ac.at (P.J. Uggowitzer), stefan.pogatscher@unileoben.ac.at (S. Pogatscher).

https://doi.org/10.1016/j.mtla.2020.100997
Received 21 December 2020; Accepted 25 December 2020
Available online 2 January 2021

slow final cooling to room temperature directly afterwards. This generates transformable clusters and nuclei of the main hardening phase $\beta$" [13]. In this respect IQ is therefore comparable to pre-aging [14], and increased mechanical parameters can be achieved in the final product [13,15,16].

In addition to the group of age-hardening elements, dispersoid-forming elements with low solubility such as Fe, Mn and Cr can be advantageously added. If primary constituents are largely suppressed during the casting process, small and densely distributed secondary phases will form during homogenization [17,18] significantly influencing the mobility of both the grain boundary and the dislocation motion [19]. Especially in Al–Mg–Si alloys, effectively stabilizing the grain boundaries turns out to be quite beneficial because processing temperatures are comparably high, thus increasing the kinetics of boundary rearrangements [20–22].

In a 2006 study Knipling et al. [23] listed several elements that form trialuminides, $Al_3X$ (X = Sc, Ti, Zr, Hf, Er, Tm, Yr and Lu), in Al alloys, of which Zirconium and Scandium have already been intensively investigated. Due to the high price of Sc and the low coarsening resistance of $Al_3Sc$, Zr may be a more attractive candidate for industrial use. To minimize the disadvantage of the prolonged annealing time necessitated by the reduced diffusivity of Zr within Al, it was shown that minor additions of Si (up to 0.18 at%) accelerate the precipitation kinetics [24]. Generally, $Al_3X$-particles are not only used advantageously in unalloyed Al [23,24], but also in age-hardenable alloy systems (2xxx [25–27] or 7xxx [28,29]) and – this has been quite prominent lately – in additively manufactured parts [30,31]. These particles were shown to have a significant impact on dislocation and grain boundary motion, which decreases recrystallization tendency and, thus, leads to the formation of subgrains. In combination with an increased amount of Orowan hardening, an increase in strength is thus observed for Sc or Zr containing 2xxx and 7xxx series alloys [32–34].

The effect of trialuminides on Al–Mg–Si alloys was recently investigated [35–38]. However, for alloys containing Si (in amounts greater than the minute nucleation agent addition shown in [24]) it was reported that Zr,Si-phases can form [39], thus decreasing the amount of Zr available for the formation of fine trialuminides dispersoids. A transformation of the beneficial metastable $L1_2$-$Al_3Zr$ precipitates (coherent with Al-matrix) into its stable $D0_{23}$-structure (incoherent with Al-matrix) is also observed at elevated temperatures (roughly around 500 °C) [40]. A high Si content such as that of Al–Mg–Si alloys was reported to favor the occurrence of an incoherent $(Al,Si)_3Zr$ phase and to cause accelerated transformation [41–43]. 6xxx-series alloys need comparably high homogenization temperatures to obtain the desired intermetallic landscape (dissolution of primary $\beta$-$Mg_2Si$, reduction of micro and macro segregation, and transformation of Al(Fe,Mn)Si-phases) [44–46], which limits the positive effects of Zr on industrially processed Al–Mg–Si alloys due to coarsening. However, investigations demonstrate that Zr additions can have a similar [47] and even additive effect [48] on recrystallization retardation comparable to conventional dispersoids containing Fe, Mn or Cr. A few Al–Mg–Si standards (EN AW-6056, EN AW-6065, EN AW-6110 and EN AW-6182) allow Zr up to a maximum of 0.20 wt% [49] to make use of these beneficial dispersoids.

In this study, following the standard production route for thick plate alloys (casting, homogenization, hot rolling and artificial aging), we combined all of the strengthening mechanisms presented in a model Al–Mg–Si plate alloy. The necessary protocol for achieving the desired high strength is as follows: (i) balanced and optimized number of age-hardenable elements (such as Si, Mg and Cu); (ii) application of interrupted quenching; and (iii) addition of Zr. It is not yet fully understood how Zr interacts with Mn and Fe or how it reacts at 6xxx-typically high processing temperatures, and the strengthening mechanism due to Zirconium in such complex alloys is also still unknown [35]. These issues are examined in detail below. The scientific methodology in this study addresses the question of whether it is possible to combine all of these strengthening mechanisms synergistically in one alloy, and whether the yield strength of Al–Mg–Si wrought thick plates can be increased to over 400 MPa.

## 2. Experimental methods

For this study, five alloys based on an EN AW-6082 were produced at a laboratory scale. After re-melting of primary industrial material (EN AW-6082) in a resistance heated furnace (Nabertherm K20/13/S), pure Si, Mg, Cu and Zirconium (in the form of AlZr10) were alloyed to obtain the compositions listed in Table 1. These were measured using optical emission spectroscopy (note that the simulation-assisted design concept is described in the next section). After refining the melt, which was held at roughly 750 °C, via Ar gas purging and grain refiner addition, casting into custom-made pre-heated molds similar to that in industry was started according to [50]. A cooling rate of 3–5 K/s was maintained. After fillet piece cutting and homogenization treatment, the resulting slabs were hot rolled from 40 mm down to 6 mm in several rolling steps. A residual amount of 0.02 wt% Cr is present in all alloys, due to the usage of scrap in the production of the industrial material.

Solution heat treatment of tensile test samples was performed using a circulating air furnace (Nabertherm N60/85 SHA) at 570 °C for 20 min. After either water quenching or interrupted quenching into a 180 °C hot metal bath (Bi57Sn43) with delayed cooling within 24 h to RT at a decreasing cooling rate, the samples underwent 14 days of natural aging to emulate industrial processing. After 7 days of natural aging, a plastic pre-deformation of 2% took place. After another 7 days artificial aging was carried out at 160 °C for 14 h with 10 h of ramping up (to simulate the heating of thick plates), resulting in a total aging time of 24 h for the water-quenched specimens (T651 state). Starting from the base alloy, artificial aging times for reaching T651-state were checked for each alloy variation and no major differences were detected. Concerning IQ specimens, 2 h aging at 160 °C was applied, *i.e.* in total 12 h (IQ state). The whole heat treatment process is schematically shown in Fig. 1. Whereas the solid black line represents a standard industrial processing scheme for hot rolled plate alloys, our high strength variants require an alteration of the homogenization strategy (dashed orange line) and tuning of the final heat treatment (IQ + shortened artificial aging), as indicated by the dashed blue line (see also Sections 3.3 and 3.4).

To characterize the mechanical parameters uniaxial tensile tests were performed on a universal testing machine (Zwick-Roell BT1) equipped with a 50 kN load cell. Round specimens were prepared with a 30 mm long and 5 mm thick gauge in accordance with EN-ISO 6892-1. As-quenched specimens were tested within 5 min of water quenching. 3 samples were tested to calculate mean value and standard deviation.

**Table 1**
Measured chemical composition of all alloys tested, Al in balance (wt%).

| | Si | Mg | Cu | Mn | Fe | Zr | Si + Mg | Si/Mg | Notes |
|---|---|---|---|---|---|---|---|---|---|
| **Base alloy – 6082** | 1.02 | 0.67 | 0.08 | 0.42 | 0.33 | 0.00 | 1.7 | 1.5 | Remolten industrial primary material |
| **6082-Si** | **1.19** | 0.70 | 0.08 | 0.44 | 0.39 | 0.00 | **1.9** | **1.7** | Addition of Si |
| **6082-Cu** | 0.98 | 0.66 | **0.29** | 0.42 | 0.33 | 0.00 | 1.6 | 1.5 | Addition of Cu |
| **6082-Zr** | 1.03 | 0.66 | 0.08 | 0.42 | 0.37 | **0.20** | 1.7 | 1.6 | Addition of Zr |
| **Optimal alloy** | **1.07** | **0.81** | **0.30** | 0.41 | 0.36 | **0.21** | **1.9** | **1.3** | Co-Add. of Si/Mg, Cu and Zr |

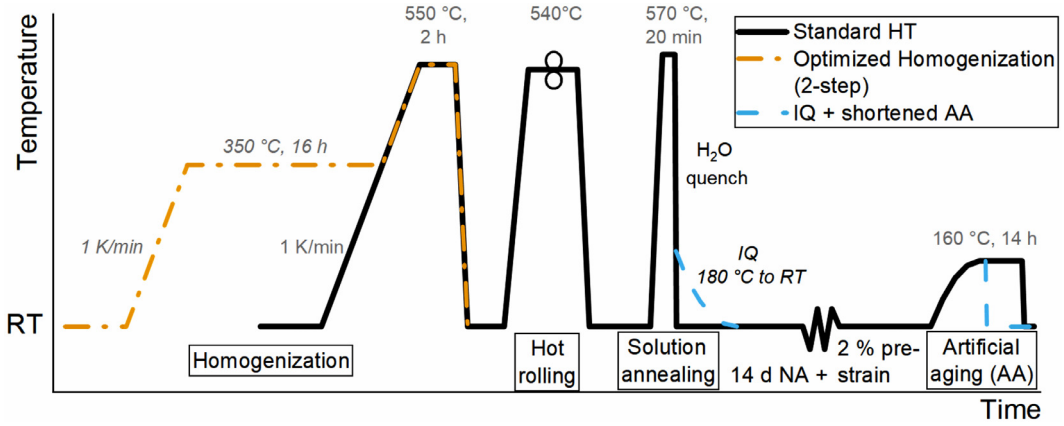


**Fig. 1.** Schematic illustration of the applied heat treatment consisting of homogenization, hot rolling, solution annealing, pre-deformation und artificial aging.

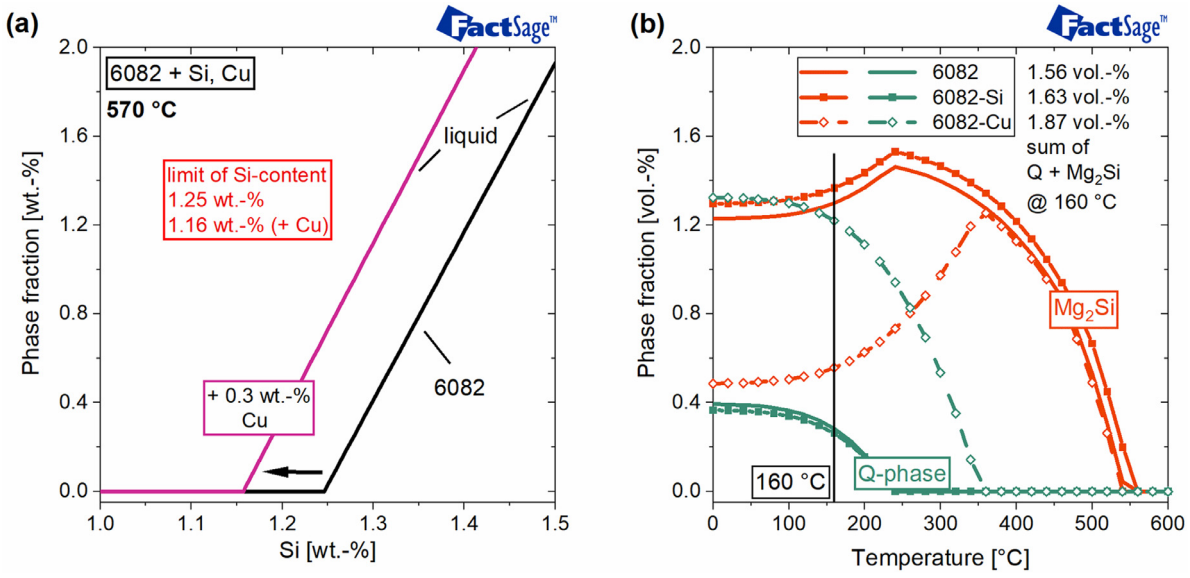


**Fig. 2.** Thermodynamic equilibrium calculations of 6082, 6082-Si and 6082-Cu (see Table 1 for chemical compositions). (a) Influence of Si and Cu content on the onset of liquid phase formation. At 570 °C annealing temperature 1.25 wt% Si is the threshold value for the occurrence of a liquid phase in the 6082 base alloy and 1.16 wt% in 6082-Cu. (b) Phase fraction of $Mg_2Si$ and Q-phase in relation to the temperature. Volumetric percentages are calculated with a density of 2.91 g/cm$^3$ for Q-phase [60] and 1.90 g/cm$^3$ for $Mg_2Si$ [61].

Thermodynamic calculations were performed with FactSage™ 7.3 and FactSage™ 8.0 software using the FACT FTLite and FACT PS databases (2020) [51,52].

To characterize the microstructure a scanning electron microscope (SEM) (JEOL 7200F FEG-SEM), equipped with an EBSD-measurement system (Nordlys Nano detector, Oxford Instruments), was deployed. Samples were prepared via a standard procedure of grinding, oxide (OPS) and electrolytic polishing. For grain boundary analysis an area of 0.5 mm$^2$ was analyzed on each sample, with a step size of 0.6 µm. The recrystallized area fraction was determined from a surveyed area of at least 2.35 mm$^2$ (step sizes of 0.6 and 3 $\mu$m) taken at t/2 representing the center of the plate. The minimum grain boundary misorientation angle was set to 5° [53] for the recrystallization analysis. Further details concerning basic EBSD data processing by means of the mtex toolbox can be found elsewhere [54–56]. Grains exhibiting a grain average kernel average misorientation (KAM) below 0.5° along with a grain average band contrast of >70 % of the maximum grain average band contrast were identified as fully recrystallized. To analyze sub-grains, grains with a minimum boundary misorientation of 0.8° were recalculated.

BSE micrographs were taken at an acceleration voltage of 5 kV and a working distance of roughly 4 mm to evaluate intermetallic dispersoid phases. Each particle's roundness is derived by dividing the actual area by the calculated circular area using the maximum diameter (the value is inversely proportional to the aspect ratio). Values close to 1 correspond to an almost perfect circular shape.

Scanning transmission electron microscope (STEM) measurements were carried out on a Thermo Scientific™ Talos F200X G2. 200 kV was taken as the acceleration voltage. Samples were cut from undeformed parts of tensile test samples. After grinding down to 100 $\mu$m, 3 mm disc specimens were prepared via a standard route consisting of grinding and electrolytic polishing with $HNO_3$ in methanol (1:3) at −20 °C and 15 V. Concerning the determination of Si containing Zr-particles the following methodology was applied. Deploying a picture analysis software (ImageJ 1.51f) and using a color threshold for the Si and Zr mapping, binary black and white pictures with particles containing Si and Zr were made. Overlapping these two by using the Boolean operation "AND" brought back a third picture where only particles were depicted that contained both Zr and Si at the same spot.

**Table 2**
Overview of mechanical parameters of all tested alloys after standard artificial aging (T651) and interrupted quenching + shortened artificial aging.

| | As-quenched | Standard AA (T651) | | | IQ + shortened AA | | |
|---|---|---|---|---|---|---|---|
| | $R_{p0.2}$ MPa | $R_{p0.2}$ MPa | $R_m$ MPa | $A$ % | $R_{p0.2}$ MPa | $R_m$ MPa | $A$ % |
| **Base alloy – 6082** | 58 ± 2 | 289 ± 3 | 309 ± 2 | 19 ± 2 | 349 ± 8 | 352 ± 9 | 11 ± 1 |
| **6082-Si** | 66 ± 2 | 319 ± 8 | 339 ± 7 | 15 ± 1 | 364 ± 4 | 373 ± 5 | 12 ± 1 |
| **6082-Cu** | 64 ± 2 | 313 ± 3 | 337 ± 3 | 17 ± 1 | 355 ± 6 | 362 ± 6 | 12 ± 1 |
| **6082-Zr** | 85 ± 0 | 334 ± 5 | 362 ± 4 | 15 ± 1 | 384 ± 7 | 398 ± 8 | 12 ± 1 |
| **Optimal alloy** | 90 ± 3 | 362 ± 9 | 392 ± 9 | 15 ± 1 | 411 ± 4 | 425 ± 4 | 14 ± 0 |

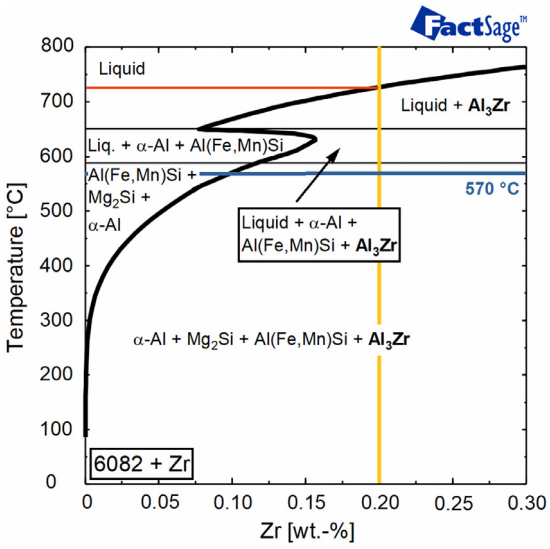


**Fig. 3.** Isopleth of 6082 with additions of Zr. The occurrence of $Al_3Zr$ is highly dependent on temperature. At the solution annealing temperature of 570 °C Zr has a solubility of about 0.1 wt% in the solid $\alpha$-Al.

## 3. Design concept

In the following we present our design concept, which is based on the exploitation of all scenarios for improving strength in a model Al–Mg–Si alloy which contains Fe and Mn. The concept involves tuning both the element composition and the processing parameters.

### 3.1. Addition and optimization of precipitation-hardening elements

As the first step in our alloy design, we adjusted the number of age-hardenable elements: Si was adjusted to Mg, and Cu was added as a strength-increasing element. The Cu amount was limited because of the decreasing corrosion resistance (especially resistance against intergranular corrosion in 6xxx-alloys [57]) associated with increasing amounts of this element [2]. After considering the option of increasing the Cu content to a corrosion-irrelevant amount of 0.3 wt%, and the specified process parameters (i.e. solution annealing temperature of 570 °C; see Section 2 and Fig. 1 for further information on the standard industrial processing route for the production of thick plates), we carried out thermodynamic calculations. The results of which are presented in Fig. 2. Fig. 2a shows the liquid phase fraction course with altered Si content in the 6082 base alloy at 570 °C. No liquid phase is allowed to form at this temperature, because otherwise the material would be unusable afterwards. A threshold Si content of 1.25 wt% can be derived from the graph (note that adding Cu to 0.3 wt% decreases the onset of liquid phase formation to an Si content of 1.16 wt%). To determine the influence of Si only this element was increased from 1.02 to 1.19 wt% in the 6082-Si alloy, but it was kept at the reference level in 6082-Cu. Mg and Si were both added to the optimal alloy to approach the preferential Si/Mg ratio of 1.2 in the main hardening phase $\beta''$ ($Mg_5Si_6$ [58,59]) (see Table 1 for the chemical compositions of all alloys).

Fig. 2b shows the phase fractions of the equilibrium phases containing Si, Mg and Cu over the temperature, which can be used as a rough estimation of the main hardening precursor phases forming during artificial aging. Adding Si increases the amount of $Mg_2Si$ considerably, without affecting the amount of Q-phase ($Al_4Cu_2Mg_8Si_6$ [60]). In the 6082-Cu alloy, a drastic rise of the Q-phase containing Cu is seen, along with a reduction of $Mg_2Si$. At 160 °C a significantly increased total hardening phase volume is present in both alloy variations (6082-Si and 6082-Cu), which should ultimately lead to an enhanced age hardening response.

### 3.2. Addition of Zirconium

Whereas Zr also precipitates from the super-saturated matrix as $Al_3Zr$, its nucleation and growth take place at much higher temperatures than those associated with the elements discussed above. Fig. 3 shows an isopleth of the 6082 base alloy with Zr up to 0.3 wt%. A maximum amount of roughly 0.1 wt% is dissolvable in $\alpha$-aluminum at the target solution annealing temperature (570 °C). Because both homogenization and hot rolling are carried out at 6xxx-typical temperatures well above 500 °C, there is a tendency to dissolution of large shares of previously formed $Al_3Zr$. Therefore, an increased amount of 0.2 wt% Zirconium addition (compared to a maximum amount of 0.15 wt% in EN AW-7050 for example [49]) was chosen. Because no primary non-hardening $Al_3Zr$ precipitates, which impair elongation, should be formed, the temperature during the casting production process was kept above 730 °C (see red line in Fig. 3).

### 3.3. Adaption of homogenization

During homogenization treatment of conventional Al–Mg–Si alloys, the dissolution of previously formed coarse $Mg_2Si$ requires a rather high temperature of about 550 °C (see Fig. 2b). Slow heating to this temperature also generates the desired formation of dispersoids. In order to form dispersoids in small sizes and high number densities, we suggest an adaptation of the homogenization treatment step. On the one hand, it is known that Al(Mn,Fe)Si-dispersoids containing Fe and Mn exhibit the highest nucleation rate at 370 °C upon heating at 0.01 K/s [62]. Conversely, an intermediate annealing step at 360 °C has been shown to promote the formation of $Al_3Zr$-nuclei and thus reduce the time needed for full precipitation at 550 °C, which is influenced by the slow diffusion of Zr [23,63]. It has also been reported that these two phase-families influence each other by promoting heterogeneous nucleation sites [64], which necessitates a holding annealing step to prevent coarsening and non-uniform distribution of dispersoids. With this in mind, optimized homogenization (indicated by the dashed yellow line in Fig. 1) was applied to the alloys containing Zr. This homogenization consisted of an intermediate holding annealing step at 350 °C for 16 h and a second step at 550 °C for 2 h.

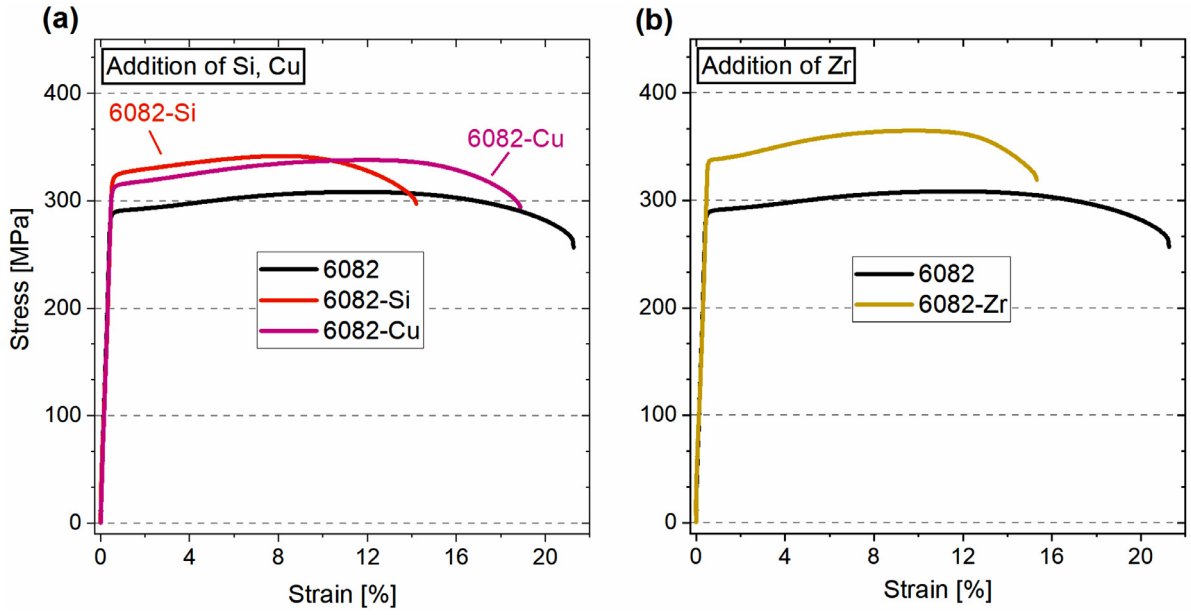


**Fig. 4.** Stress–strain curves of (a) the base alloy 6082, 6082-Si and 6082-Cu and (b) 6082-Zr in T651 state

### 3.4. Interrupted quenching

Because Al–Mg–Si alloys lose their age hardening potential due to natural aging [11,12], quenching to an elevated temperature was applied as an additional measure to all the experimental alloys tested here [13]. Accordingly, all samples were quenched to 180 °C right after solution annealing and slowly cooled to room temperature (this takes 24 h in total, at a decreasing cooling rate) to simulate the cooling of thick plates (indicated by the dashed blue line in Fig. 1). This should lead to the formation of favorable clusters and nuclei of the main hardening phase $\beta''$, and is comparable to pre-aging [13,14]. Because this treatment already precipitates many of the age-hardenable elements, a shortened final artificial aging step was applied.

## 4. Results

This section builds on the measures presented in Section 3, which addressed alloy and process design, and optimal alloy and microstructure characterization. As an overview, Table 2 lists the most important stress–strain curve values for the aged samples presented below. All alloys were also tested right after solution annealing in the as-quenched state. These values are also listed in Table 2 and are discussed in Section 5.

### 4.1. Alloy design

#### 4.1.1. Addition and optimization of precipitation-hardening elements

Fig. 4a shows the stress strain curves of alloys optimized by adding Si or Cu in comparison with the base alloy 6082 in the fully strengthened T651 state. Regarding mechanical properties, both measurements (Si/Cu addition) generate a considerable increase in strength. Whereas 6082-Cu shows a total yield strength increase of 24 MPa, adding Si results in an increment of 28 MPa. Elongation to fracture is significantly reduced in 6082-Si. 6082-Cu shows hardly any changes in this respect.

#### 4.1.2. Addition of Zirconium

Fig. 4b shows the stress–strain curves of the alloy with a Zr addition compared to the 6082 base alloy in T651 state (6082-Zr was homogenized by 2-step treatment). The achievable property changes generated by adding Zr are quite remarkable. A significant increase in yield strength of roughly 45 MPa is observed. The elongation to fracture stays high at around 15%. Note that a similar effect on mechanical parameters is achieved when using pure Al instead of industrially produced EN AW-6082 as base material (see Supplementary Material: Table S1 and Fig. S1).

### 4.2. Process design

#### 4.2.1. Adaption of homogenization – formation of dispersoids

Fig. 5 shows SEM-backscattered electron (BSE) micrographs, where all dispersoids containing Fe, Mn, Cr and Zr appear as bright dots (Fig. 5a–d) after one-step and two-step homogenization treatment in the undeformed state before hot rolling for 6082 and 6082-Zr. The corresponding particle distribution statistics are shown in Fig. 5e and f. In Fig. 5a-d. The number densities of all particles after homogenization show the following trends (see Fig. 5f): (i) the number density increases when Zr is added; (ii) for both alloys the number density increases when switching from one- to two-step homogenization; (iii) two-step homogenization applied to the base alloy 6082 generates a higher number density than standard one-step homogenization of the 6082-Zr alloy. Compared to the material containing Zr, an increased number of elongated particles (0–0.33 roundness; see Section *2 Experimental methods*, for an explanation of this term) forms in the base alloy 6082, especially after one-step homogenization. With two-step homogenization the number of round particles (with an even smaller diameter; see Fig. 5e) is more than doubled. Generally, two-step homogenization leads to an overall decrease in the diameter of all particles in 6082 (from 116 nm to 85 nm). In 6082-Zr the diameter of the particles stays on a level comparable to any homogenization (between 70 and 80 nm), especially in the most important fraction of roundish, small particles (0.66–1.00 roundness). However, the number density increases significantly with two-step homogenization, as also reported in Ref. [63]. Fig. 5g and h show the distribution of particles after hot rolling and solution annealing at 570 °C in T4 state. The number densities are reduced in both alloys. In particular, the complete disappearance of strongly elongated particles (0–0.33 roundness) and a strong reduction in the second share of particles (0.33–0.66 roundness) is also apparent in both. Whereas the mean diameter of all particles increases from 85 to 101 nm in 6082, no alteration in the particle size is seen for 6082-Zr (Fig. 5i).

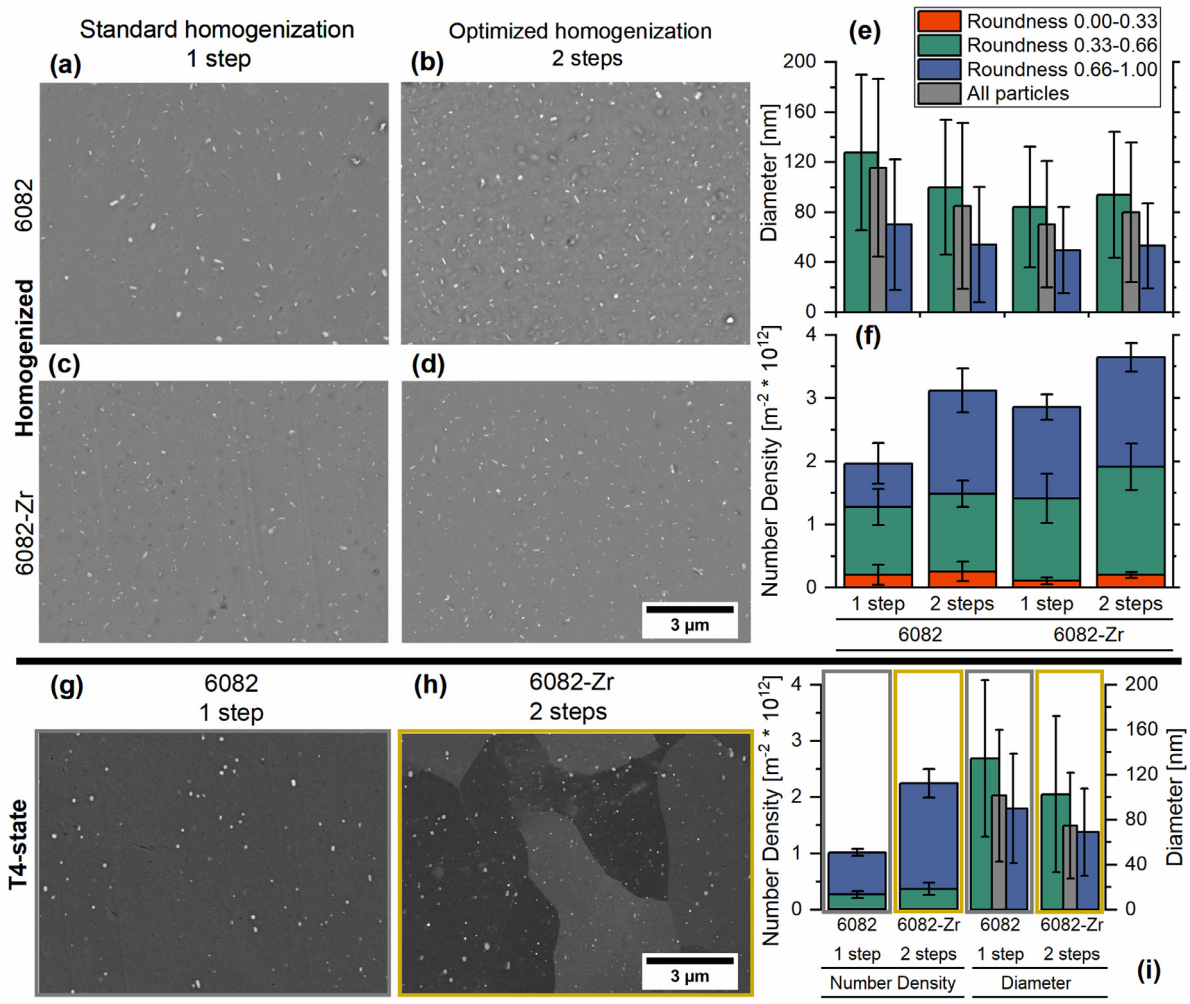


**Fig. 5.** SEM-BSE micrographs of the microstructure in different states (after homogenization – a–e; in T4-state – g–i) after one-step homogenization (a, c, g) and two-step homogenization (b, d, h) of the base alloy 6082 (a, b, g) and 6082-Zr (c, d, h). Mean diameter (e, i) and number densities (f, i) of all detected dispersoids are categorized in three groups according to their shape.

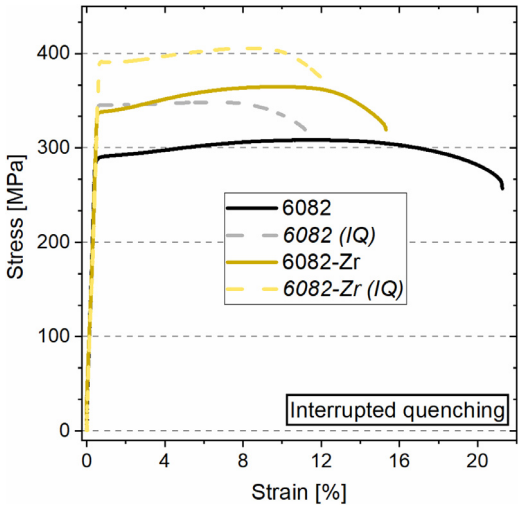


**Fig. 6.** Stress–strain curves for 6082 and 6082-Zr in T651 state and after interrupted quenching. In both cases an increase in yield strength of about 40 to 50 MPa is observed.

#### 4.2.2. *Interrupted quenching*

Fig. 6 shows stress strain curves for 6082 (one step homogenization) and 6082-Zr (two-step homogenization) after standard AA (T651 state) and interrupted quenching + shortened AA (160 °C/2 h). This treatment generated an increase in yield strength of about 40 to 50 MPa for both alloys. Obviously this process variation not only strengthens the base alloy, but also – almost equally – 6082-Zr, which demonstrates that IQ and the effect of Zr addition work synergistically.

### 4.3. *Optimal alloy*

After demonstrating the gain in strength caused by applying the individual measures presented, we now investigate whether these can be combined to create an optimal alloy. The measures consist of (i) a maximum dissolvable amount of Si adjusted to Mg, combined with the addition of 0.3 wt% Cu; (ii) the addition of 0.2 wt% Zr; and (iii) the application of IQ to suppress both the formation of non-hardening phases and, subsequently, the loss of hardening potential. Fig. 7 shows the results of this last alloy design step. Compared to the reference alloy, the sum of measures (i) and (ii) generates a yield strength increase of 73 MPa. Interrupted quenching further increases strength by 49 MPa (light green dashed curve in Fig. 7), resulting in a significantly increased yield strength of 411 MPa, as compared to commonly processed EN AW-6082 reference plate material with 289 MPa yield strength. Note that

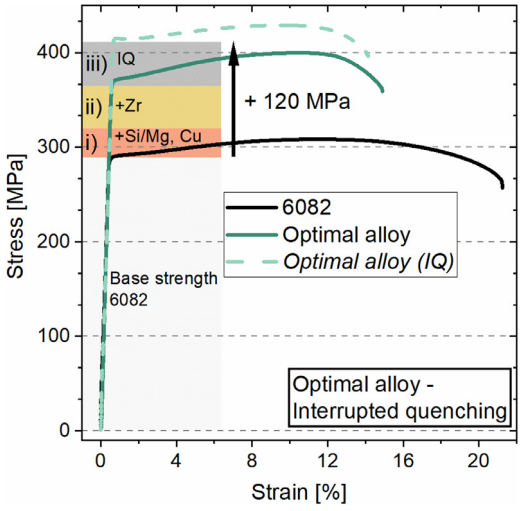


**Fig. 7.** Demonstration of an optimal strategy for high strength plate material via stress–strain curves. The minute optimization of chemical composition and modified industrial processing can boost the yield strength of today's state-of-the-art EN AW-6082 plate material by more than 40%.

these effects can also be achieved using pure Al as the base material (see supplementary material: Table S1 and Fig. S1).

### 4.4. Microstructure analysis

#### 4.4.1. 6082-Zr

Fig. 8 shows the results of SEM-EBSD measurements of the base alloy 6082 and 6082-Zr. A depiction of the 3rd order KAM (step size 0.6 µm, threshold 5°) in Fig. 8a and b highlights the noticeable difference between these two alloys after solution annealing at 570 °C. Whereas only little deformation is stored in 6082 after solution annealing, misorientation is still high in 6082-Zr. This can also be seen from Fig. 8c and d, which shows the band contrast for each specimen. A further depiction is found in the supplementary Fig. S2a and b, where recrystallized areas are shaded in blue. The distribution of all boundaries for these two alloys in Fig. 8e and f further confirms the significant difference in the microstructures presented. No sharp transition of small angle grain boundaries (SAB) and high angle grain boundaries is evident. However, McQueen defines SAB up to a threshold value of 8° [5], Gottstein until 15° [65]. Exemplarily taking the latter value of 15°, there is a roughly uniform distribution in 6082, whereas in 6082-Zr the vast majority of grain boundaries (88%) are measured at under 15°.

#### 4.4.2. Optimal alloy

Fig. 9 shows the microstructure of the optimal alloy after standard AA containing several different types of dispersoids. Two distinct phase families are present: (i) phases containing Fe, Mn and Cr (Fig. 9b–e) and (ii) phases containing Zr (Fig. 9g–i). Fig. 9b–e shows that Fe, Mn and Cr are all mixed and do not precipitate on their own, which confirms these particles as Al(Fe,Mn,Cr)Si-phases. In contrast, Zr (see Fig. 9g and h) either forms pure $Al_3Zr$-precipitates or a substitution of a certain amount of Al by Si takes place to form $(Al,Si)_3Zr$ (a few examples are indicated by red arrows). Of all detected phases containing Zr, 62% had a detectable amount of Si (see Fig. 9g–i). Fig. 9i also shows that Zr-particles are often attached to Al(Fe,Mn,Cr)Si-particles, which indicates heterogeneous nucleation (for better visibility only Mn was selected in multi-element EDX mapping). Note that using various tilting angles in the STEM confirmed that these two phases are located on each other (see supplementary material Fig. S3). The size distribution in Fig. 9f indicates that the Zr particles are much smaller (74 ± 32 nm) than the other type of dispersoid (134 ± 72 nm). Although the cumulative sum of the Fe, Mn and Cr content (0.38 at%) is more than six times higher than Zr (0.06 at%), the areal density of $(Al,Si)_3Zr$ is more than twice as high ($7.52 \times 10^{12}$ m$^{-2}$ compared to $2.97 \times 10^{12}$ m$^{-2}$).

Fig. 10a shows a dark field STEM micrograph with bright particles along dislocations and entangled dislocations that tend to be stuck to these particles. The multi-element mapping in Fig. 10b shows Mn containing as well as Zr containing dispersoids and Mg and Si rich hardening phases. Heterogeneous precipitation of the two dispersoid-phases is also observed in this micrograph (as in Fig. 9h), as well as a tendency towards the formation of the main hardening particles on dispersoid phases (indicated with red arrows in Fig. 10b). Besides the nucleation on the phase boundaries of such particles, coarsened phases containing Mg and Si are observed along dislocations (indicated by dashed yellow lines in Fig. 10b). This is depicted in more detail in Fig. 10c–f.

Fig. 11 shows several STEM micrographs of a sub-grain with an orientation close to the <001>-axis of the optimal alloy (indicated by the red circle in Fig. 11a). In Fig. 11a and b many bright constituents, identified as either Zr- or Mn-rich (Fig. 11b), are located exactly at the border of the sub-grain in the middle of the picture (indicated by the yellow and red arrows along the grain boundary). This indicates the interference of these particles with sub-grain boundaries. The dark-field micrograph of the optimal alloy in Fig. 11c reveals that many dislocations are pinned inside sub-grains by dispersoids (see red circle).

## 5. Discussion

As the above data shows, altering the chemical composition (age-hardenable elements Mg, Si and Cu; Zr as dispersoid former) and adapting the heat treatment (optimized homogenization and interrupted quenching) generated an exceptionally high yield strength of over 400 MPa in an optimal 6082-type plate alloy. In the following we discuss the underlying mechanisms which caused this gain in strength. We also provide a detailed analysis of the role played by minor Zr addition in microstructure evolution.

### 5.1. Influence of Si and Cu addition

Adding Si and Cu is known to cause an increase in strength via solid solution strengthening and precipitation strengthening [66]. Table 3 shows the mechanical parameters of the alloys tested here in different states while undergoing standard artificial aging. Right after quenching ("As-quenched") only a minor difference in yield strength is measured. In the absence of any hardening phases this difference can be attributed solely to solid solution hardening caused by different Si and Cu content [10]. However, according to the model of solid solution hardening by Leyson et al. [67] we calculate a relative strength difference of less than 1 MPa to be caused by the alterations in 6082-Si and 6082-Cu [10]. Therefore this increase in the as-quenched strength is attributed to clusters, which form either during quenching or during the very short period of less than 5 min between quenching and tensile testing [10,68]. Concerning artificial aging, both alloy variations show an enhanced strength response of roughly 20 MPa. From Fig. 2b it is qualitatively seen that adding Si and Cu generates an increased volume fraction of strengthening phases at 160 °C (1.56 vol% in the reference, 1.63 vol% in 6082-Si and 1.87 vol% in 6082-Cu), from which an increased precipitation pressure and thus an increased hardening effect can be derived.

### 5.2. Influence of Zr addition

Adding Zr to the base alloy 6082 results in a strength increase of 28 MPa in the as-quenched state after hot rolling (6082-Zr). Artificial aging causes a further increase in yield strength (17 MPa), which generates a total increase of 45 MPa in the fully hardened T651 state compared to 6082. Further alloying with Si, Mg and Cu in the optimal alloy shows an additive effect (increased yield strength in the T651 state of 73 MPa compared to 6082). To attribute these findings to the corresponding mechanisms, a detailed investigation of the microstructure,

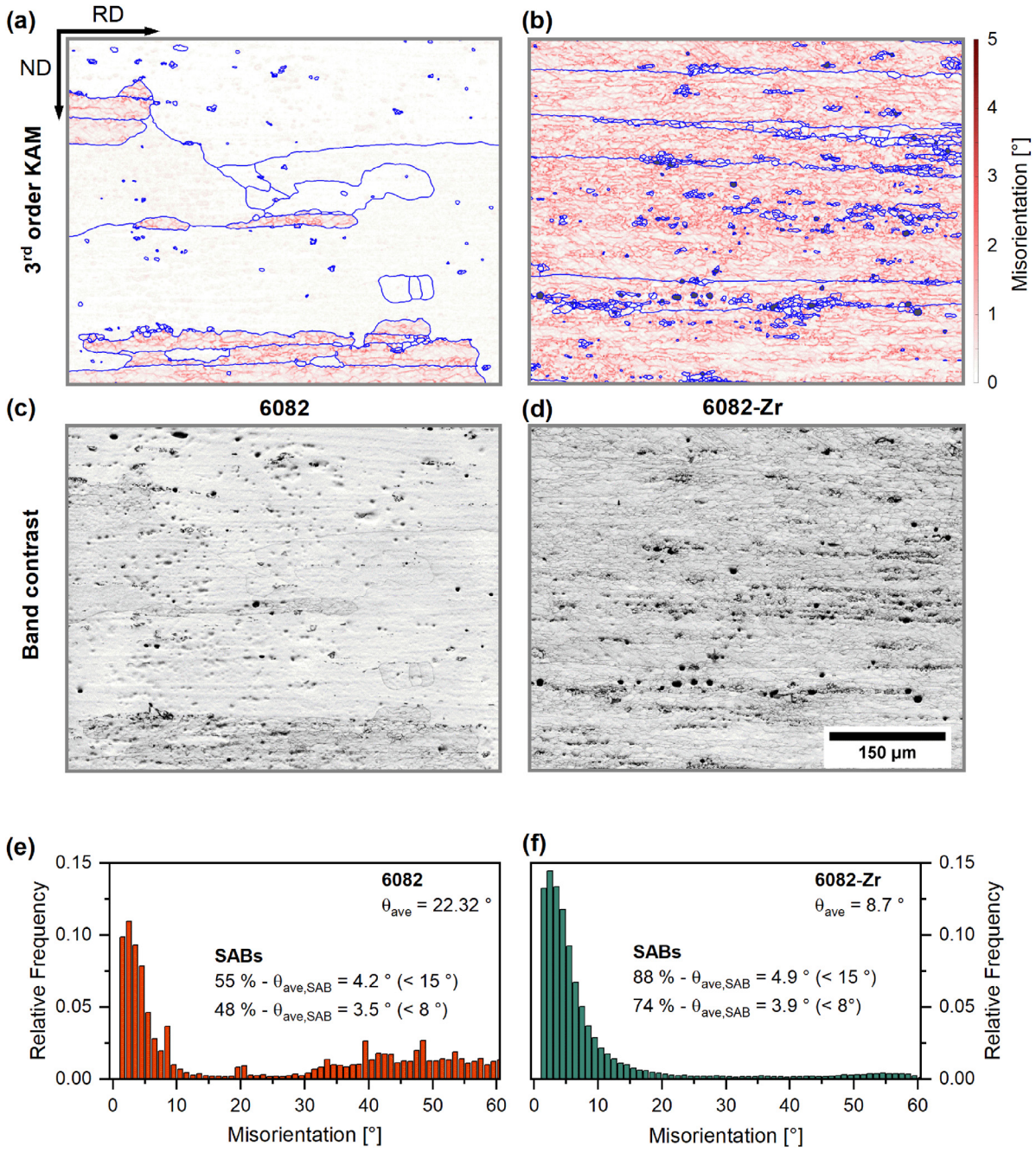


**Fig. 8.** Comparison of the microstructure in T4 temper after solution annealing (570 °C for 20 min) of 6082 (a, c, e) and 6082-Zr (b, d, f). a, b) 3rd order kernel average misorientation up to a KAM threshold of 5°. Boundaries above 5° are shown in blue, as well as larger non-indexed areas. (c, d) Depiction of the band contrast. (e, f) Misorientation distribution of all measured boundaries; infos on the threshold used can be found in the text.

**Table 3**
Overview of strength values of all alloys tested in different states for standard AA. Data were acquired right after solution annealing and quenching (as-quenched) and after final artificial aging treatment (all values in MPa). Solid solution hardening is calculated according to [67]. The contribution due to artificial aging is calculated as the difference between as-quenched strength and strength in the T651 state.

| | As-quenched | | Artificial aging | | T651 (conv. AA) |
|---|---|---|---|---|---|
| | $R_{p0.2}$ | Gain to the base alloy | Strength gain | Gain to the base alloy | $Rp_{0.2}$ |
| **Base alloy – 6082** | 58 ± 2 | | + 232 ± 3 | | 289 ± 3 |
| **6082-Si** | 66 ± 2 | 8 ± 3 | + 253 ± 8 | + 21 ± 9 | 319 ± 8 |
| **6082-Cu** | 64 ± 2 | 7 ± 3 | + 249 ± 3 | + 17 ± 5 | 313 ± 3 |
| **6082-Zr** | 85 ± 0 | 28 ± 2 | + 249 ± 5 | + 17 ± 6 | 334 ± 5 |
| **Optimal alloy** | 90 ± 3 | 32 ± 3 | + 272 ± 10 | + 40 ± 11 | 362 ± 9 |

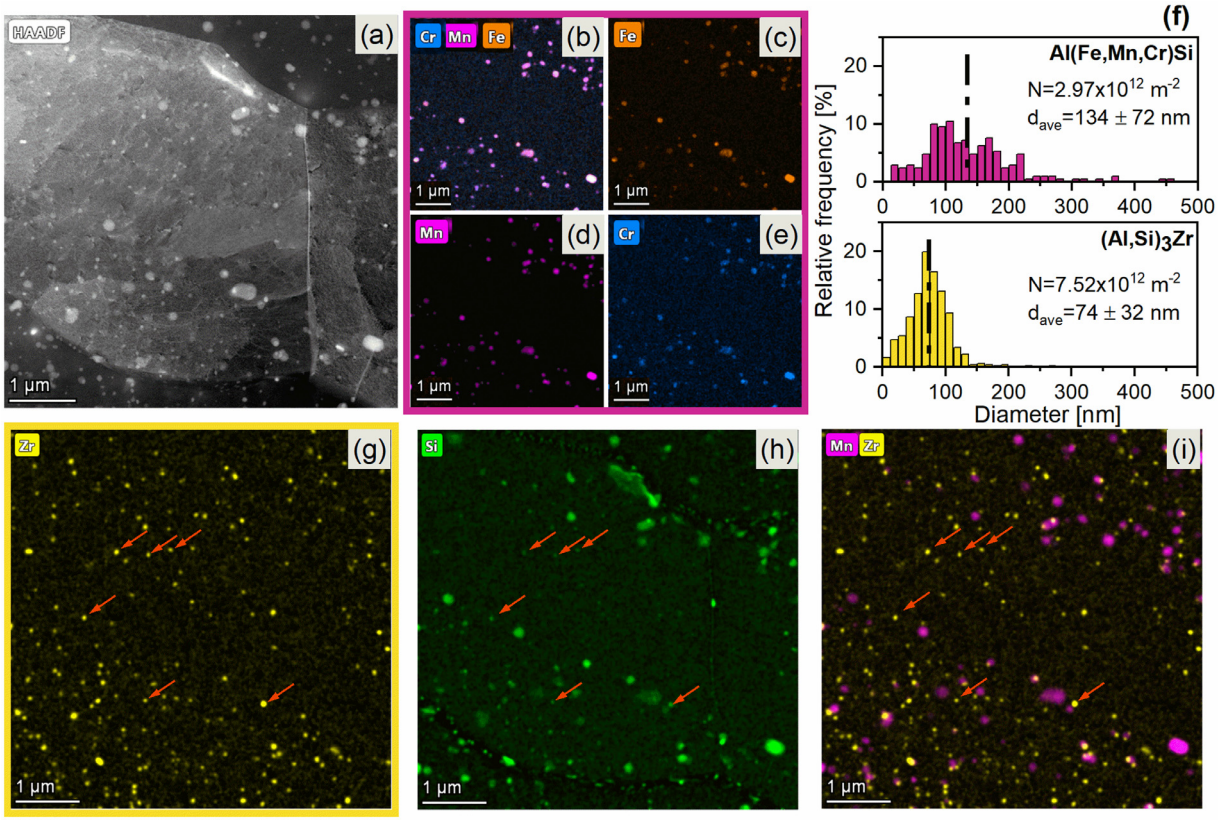


**Fig. 9.** STEM-EDX micrographs of the dispersoid landscape of the optimal alloy in condition T651. (a) HAADF-overview of the microstructure. (b-e) EDX mapping of FeMnCr (b), Fe (c), Mn (d) and Cr (e). (f) Particle distribution of FeMnCr-phases and $(Al,Si)_3Zr$-phases. The dash-dotted line represents the mean diameter. (g–i) EDX mapping of Zr (g), Si (h) and MnZr (i). The red arrows indicate particles that contain both Si and Zr.

which considered the dispersoids in particular, was carried out. Both of the alloys containing Zr are discussed below.

*5.2.1. Formation of dispersoids*

Adding Zr leads to the formation of $Al_3Zr$. Here almost two-thirds of all precipitates show that a substitution of Al by Si forms $(Al,Si)_3Zr$ (see Fig. 9i) in the optimal alloy. For both the Zr-free base alloy 6082 and 6082-Zr, the optimized 2-step homogenization has proved effective in creating a dispersoid landscape with an increased number density and decreased average diameter of all particles (see Fig. 5). STEM measurements (see Fig. 9h) have confirmed previous observations of heterogeneous nucleation of Mn- and Zr-rich particles on each other in the optimal alloy [64,69].

*5.2.2. Effect of Zr on the microstructure*

SEM-EBSD measurements in Fig. 8 reveal completely different microstructures in the base alloy and 6082-Zr. The cause lies in quite different dispersoid landscapes and the increased number density of smaller particles in 6082-Zr (see Fig. 5) due to both the Zr addition and an optimized homogenization strategy. It is known that such second phase particles interfere with moving grain boundaries and block their movement during recrystallization, and other processes that include a boundary rearrangement [70]. Dispersoids, such as $Al_3Zr$ that have a coherent interface with the matrix are postulated to have a retarding pressure on boundaries which is twice as high as incoherent ones. Nevertheless it is quite remarkable that the incoherent Mn-dispersoids do not inhibit recrystallization more effectively (Fig. 8c), even though the reference alloy actually contains sufficient levels of Mn (0.42 wt%) to act well against grain boundary and dislocation movements [20,71]. The standard homogenization one-step treatment, however, causes the formation of comparatively coarse particles with low number density. This results in a less effective retarding pressure against recrystallization in the base alloy, thus rendering the Mn addition fairly ineffective.

*5.2.3. Influence on mechanical parameters*

In the as-quenched state, 6082-Zr, which is modified by Zr-addition only, shows a strength increase of 28 MPa compared to the base alloy. Dispersoids typically contribute to a strength increase via Orowan hardening, due to typical sizes, which forecloses them to be cut by dislocations [10,35]. Strength contributions of Zr-particles according to the Orowan mechanism calculated according to [9] are given in Table 4, and are only of minor importance. In 6082-Zr only 10 MPa and in the optimal alloy only 14 MPa are calculated in addition to the base alloy. Assuming that particles containing Zr that precipitate heterogeneously at present Mn-rich dispersoids (counted in the calculation for the optimal alloy separately) do not contribute much to increased strength, this value is reduced even further. Consequently, the Orowan mechanism alone cannot explain the increase in strength caused by adding Zr.

Following the standard production route of thick plates, hot rolling at 540 °C was applied for all alloys tested. Due to the high stacking fault energy of Al, sub-grains can easily form during this production step. More severe conditions (increase of deformation speed $\dot{\varepsilon}$ and decrease of temperature T) generate a decrease in the sub-grain size [5,73]. After hot rolling, similar elongated microstructures, indicating non-recrystallized areas, are present in both the reference alloy and in 6082-Zr (Fig. S4). As already described above, recrystallization in 6082-Zr is suppressed during solution annealing due to the beneficial dispersoid landscapes, resulting in a largely recovered microstructure. We can therefore expect sub-grain boundary hardening as an additional strengthening mechanism in the alloys containing Zr.

An evaluation of the microstructure in the optimal alloy shows an average sub-grain size ($\delta$) of roughly 5 $\mu$m in rolling direction (equiv-

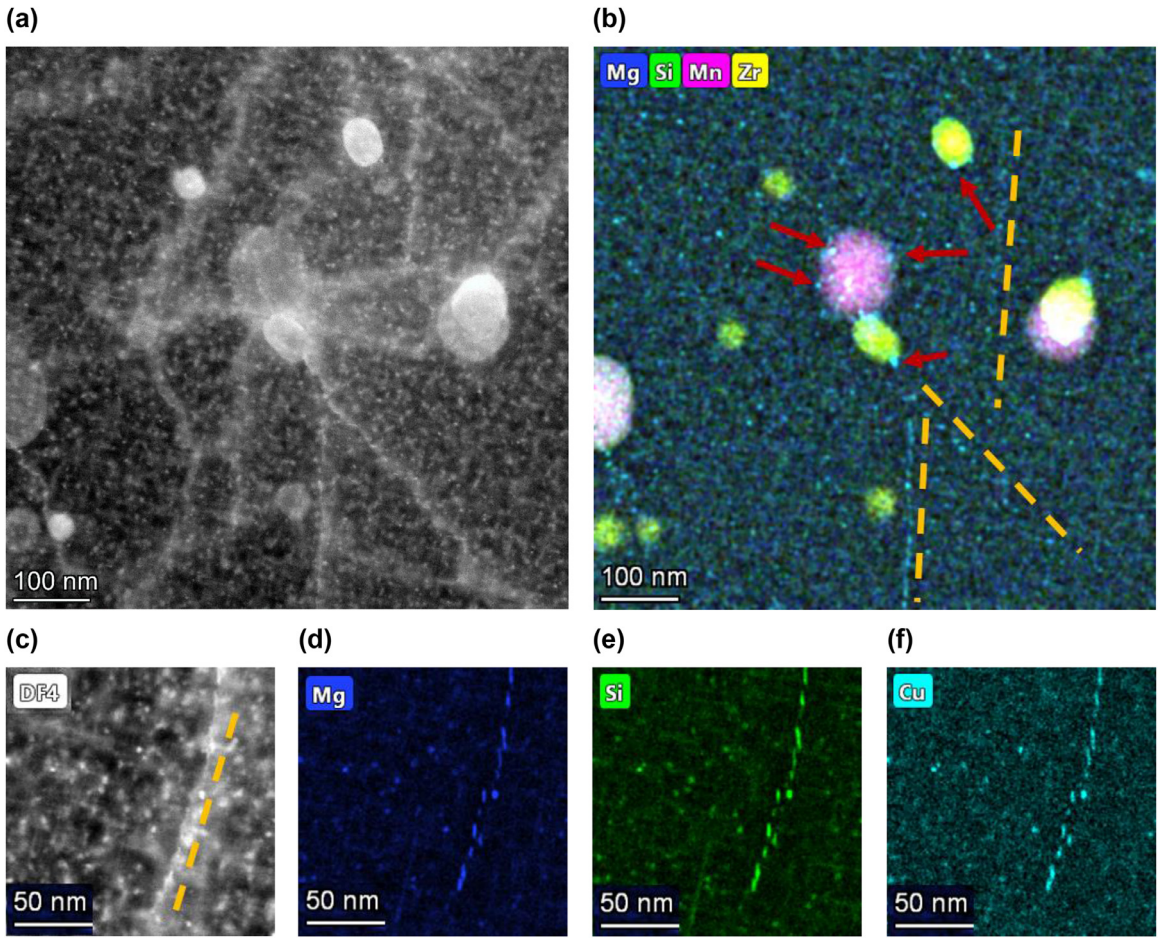


**Fig. 10.** STEM micrographs of the optimal alloy in the T651-state. (a) Dark field micrograph showing dispersoids along with entangled dislocations. (b) EDX-mapping of Mg, Si, Mn and Zr which shows the heterogeneous nucleation of several phases (hardening phase containing Mg, Si on dispersoids indicated by red arrows) and a tendency towards precipitation of the hardening phase on dislocations (see dashed yellow line). This can also be seen in more detail in c–f.

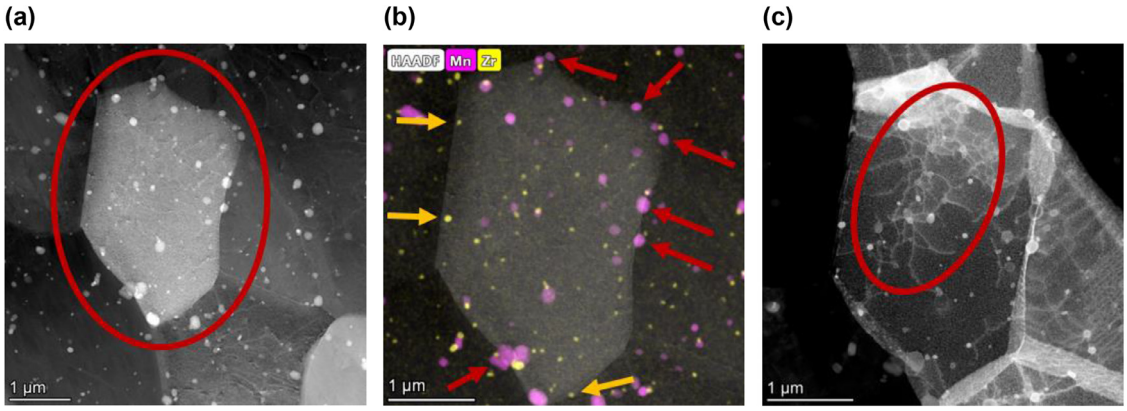


**Fig. 11.** STEM micrographs of the optimal alloy in the T651-state. The grain in the middle (light greyish grain, indicated by a red circle) in (a) is near the <001>-axis. (a) HAADF micrograph showing small sub-grains with a size of roughly 3–5 $\mu$m and dispersoids. (b) Multi-element EDX mapping of the sub-grain (grain from (a), circled in red) in the <001>-axis. Many particles (indicated by arrows) are located right on the boundary. (c) Dark-field micrograph showing the dislocation distribution. An entanglement of dislocations can be observed in the vicinity of bright particles (red circle). Sub-grain boundaries are made up of a high number of stacked dislocations.

alent to the testing direction). Putting this into Eqs. (1) and (2), which were developed by Ginter and Farghalli [74], with a burgers vector (b) of $2.86 \times 10^{-10}$ m, a shear modulus (G) of 25.4 GPa and a Taylor factor (M) of 3 gives a strength increase ($\Delta\sigma$) of 44 MPa due to sub-grain boundary hardening [74]. Taking into account that – depending on the threshold value (see 4.4.1 6082-Zr) – 74% or 88% of the total boundaries are made up of SAB (Fig. 8f), this increment is reduced to a value between 33 and 39 MPa. Heterogeneous nucleation of 50% of all Zr-containing particles (Fig. 9i) leads to a considerable reduction of their hardening contribution. Reducing Orowan hardening to about half the amount would leave 33 MPa for the optimal alloy, which is only 3 MPa higher than in the base alloy. Therefore this contribution judges to be not significant and

**Table 4**
Simulated strength contributions due to Orowan hardening of the reference, 6082-Zr and optimal alloy (all values in MPa). Calculated according to [10].

| | T651 (conv. AA) | Total dispersoids strengthening (calculated) | | Input parameters | |
|---|---|---|---|---|---|
| | $R_{p0.2}$ | Al(FeMnCr)Si | $(Al,Si)_3Zr$ | Diameter [nm] | Volume fraction [$m^3/m^3$][a] |
| **Base alloy – 6082** | 289 ± 3 | 30 | – | SEM (**Fig. 5**g)<br>101 ± 59 | 0.0090 |
| **6082-Zr** | 334 ± 5 | 40 | | SEM (**Fig. 5**h)<br>75 ± 47 | 0.0115[b] |
| **Optimal alloy** | 362 ± 9 | 23 | 21 | STEM (**Fig. 9**b and d)<br>134 ± 72 (Mn)<br>74 ± 32 (Zr) | 0.0093 (Mn)<br>0.0024 (Zr) |

[a] The volume fraction is calculated by using the at% of Mn and Zr and assuming that all of it precipitates as $Al_{12}Mn_2FeSi$ [72] or as $Al_3Zr$ [35]. Therefore this value represents the maximum amount, because not all Mn or Zr will precipitate entirely during processing.
[b] The volume fraction of the dispersoids in 6082-Zr is the sum of the particles containing Mn and Zr. Therefore the diameter used here does not differentiate between these two different phases.

**Table 5**
Overview of mechanical parameters of all alloys tested for interrupted quenching (all values in MPa).

| | T651 (conv. AA) | Interrupted quenching + shortened AA (2 h/160 °C) | |
|---|---|---|---|
| | $R_{p0.2}$ | $R_{p0.2}$ | Strength gain |
| **Base alloy – 6082** | 289 ± 3 | 349 ± 8 | 60 ± 9 |
| **6082-Si** | 319 ± 8 | 364 ± 4 | 45 ± 9 |
| **6082-Cu** | 313 ± 3 | 355 ± 6 | 42 ± 7 |
| **6082-Zr** | 334 ± 5 | 384 ± 7 | 50 ± 8 |
| **Optimal alloy** | 362 ± 9 | 411 ± 4 | 49 ± 10 |

the measured increase in yield strength listed in Table 3, of 28 MPa in 6082-Zr and 32 MPa in the optimal alloy, is mostly attributed to subgrain boundary hardening (as-quenched strength gain without contribution of artificial aging). Additional alloying with Si/Mg and Cu does not significantly influence the as-quenched strength; see Section 5.1.

$$\frac{\delta}{b} = 10 \cdot \left(\frac{\tau}{G}\right)^{-1} \tag{1}$$

$$\Delta\sigma = M \cdot \tau \tag{2}$$

Now we consider the strength gain caused by artificial aging of the alloys containing Zr, 6082-Zr and the optimal alloy. Table 3 shows enhanced values due to artificial aging (+ 17 MPa) for 6082-Zr compared to the base alloy. Because the number of age-hardenable elements is not altered in 6082-Zr, an additional mechanism is proposed here. We note that during the 14 days of natural aging a plastic pre-deformation of 2% was applied, which generated a strain (dislocation) hardening of approximately 39 MPa. The research of Gruber et al. [75] showed that during aging at 185 °C a significant reduction of the dislocation density takes place in lean Al–Mg–Si alloys. Such softening can also be assumed to occur during artificial ageing (160 °C/14 h) of the base alloy. Because the modified dispersoid landscape present in 6082-Zr is capable of preventing dislocation motion (see Fig. 11), therefore preventing annihilation of dislocations, a strength decrease due to a reduction in the dislocation density is at least partly suppressed. The same applies to the optimal alloy.

Summing up the individual strength gains achieved by adding Si (6082-Si, 21 MPa), Cu (6082-Cu, 17 MPa) and Zr (6082-Zr, 17 MPa), a maximum increment of roughly 55 MPa should be reached during artificial aging in the optimal alloy, provided these mechanisms act additively. However, it is seen that both dispersoids (Fig. 10b) and dislocations (Fig. 10d–f) act as heterogeneous precipitation sites in the optimal alloy. On the one hand, hardening particles precipitated on dispersoids do not contribute much to the overall strength, but decrease the hardening potential. On the other hand, it can be assumed that hardening particles nucleating on dislocations tend to coarsen faster, probably due to pipe diffusion along dislocations. It is seen that the size of particles differs distinctly according to whether they lie on or next to dislocations in Fig. 10d–f. Consequently, the hardening potential is weakened as particles grow bigger. Some of the Cu content is also incorporated into $(Al,Si)_3Zr$ [26,76], which lowers the Cu content available for precipitation formation as well. This explains why the measured gain in the optimal alloy caused by artificial aging compared to the base alloys is actually a bit lower than 55 MPa, showing an increase in yield strength of 40 MPa.

### 5.3. Interrupted quenching

The third measure for increasing the strength of Al–Mg–Si alloys, interrupted quenching during solution annealing, also proved successful (for mechanical parameters see Table 5). When quenching the alloys to an elevated temperature (180 °C) and slowly cooling them to RT, which simulates the cooling of thick plates (roughly 100 mm thickness) in ambient air, a minimum strength increase of 42 MPa could be seen in all alloys compared to the conventional T651 state. Previous investigations showed that unfavorable clusters form during RT storage, caused by the high level of super-saturated solutes and quenched-in vacancies at the end of solution annealing. This decreases the artificial aging response [77,78]. By applying interrupted quenching we exploited the advantageous state of the alloy right at the end of solution annealing to promote the formation of densely distributed nuclei for $\beta$'' or directly transformable precursors [13]. This processing method works for any alloy variation and prompted a further increase in strength, finally reaching a yield strength of 411 MPa in the optimal alloy.

## 6. Conclusions

This study investigates measures for significantly increasing the strength of an EN AW-6082 alloy, which is processed according to an industrial scheme for the production of thick plates. The most important findings are summarized as follows:

- A thermodynamic simulation-based adjustment of age-hardenable elements generates a strength increase of ~ 40 MPa.
- Interrupted quenching (IQ) can increase the strength by at least 42 MPa.

- Adding 0.2 wt% Zr generates a strength increase of 45 MPa. This can be attributed to reduced recovery and recrystallization dynamics due to an increased dispersoid density. Thermally very stable sub-grain-boundary hardening was detected as the major mechanism, which was still active after hot rolling and a solution heat treatment even at 570 ˚C.

The combination of these measures results in a superior yield strength of 411 MPa, the result being an attractive new Al–Mg–Si alloy for high-strength application in the whole mechanical engineering sector. Our findings suggest that it may be possible to combine the measures presented here by modular principle to reach the desired strength in any Al–Mg–Si alloy.

## Author contributions

F.S., S.P. and P.J.U. conceived the study. F.S. produced the samples and conducted the mechanical testing. T.K. and I.W. performed the measurements. I.W. and F.S. analyzed the data. S.P. and P.J.U. coordinated and supervised the work. All authors discussed the data extensively. F.S. wrote the manuscript with the support and correction of all other authors.

## Data availability

The raw/processed data required to reproduce these findings cannot be shared at this time because the data also forms part of an ongoing study.

## Declaration of Competing Interest

The authors declare that they have no known competing financial interests or personal relationships that could have appeared to influence the work reported in this paper.

## Acknowledgments

Financial support from the Christian Doppler Research Association, the Austrian Federal Ministry for Digital and Economic Affairs and the National Foundation for Research, Technology and Development is gratefully acknowledged. The authors also wish to express their sincere thanks to AMAG rolling GmbH for the supply of alloy material. Financial support from the Austrian Research Promotion Agency (FFG) in the project 3DnanoAnalytics (FFG-No. 858040) is also gratefully acknowledged. MAT and SP are grateful for the European Research Council (ERC) excellent science grant “TRANSDESIGN” through the Horizon 2020 program under contract 757961.

## Supplementary materials

Supplementary material associated with this article can be found, in the online version, at doi:10.1016/j.mtla.2020.100997.

## References

[1] J. Hirsch, Aluminium in innovative light-weight car design, Mater. Trans. 52 (2011) 818–824.
[2] F. Ostermann, Anwendungstechnologie Aluminium, Springer-Verlag, Berlin Heidelberg, 2014.
[3] A. Poznak, D. Freiberg, P. Sanders, Automotive wrought aluminium alloys, in: R. Lumley (Ed.), Fundamentals of Aluminium Metallurgy, Elsevier, 2018, pp. 333–386.
[4] M.F. Ashby, Materials Selection in Mechanical Design, 4th ed., Elsevier, Amsterdam, 2011.
[5] H.J. McQueen, S. Spigarelli, M.E. Kassner, E. Evangelista, Hot Deformation and Processing of Aluminum Alloys, CRC Press, Boca Raton, 2011.
[6] O. Engler, J. Hirsch, Texture control by thermomechanical processing of AA6xxx Al–Mg–Si sheet alloys for automotive applications – a review, Mat. Sci. Eng. A 336 (2002) 249–262.
[7] M.W. Zandbergen, Q. Xu, A. Cerezo, G.D.W. Smith, Study of precipitation in Al–Mg–Si alloys by atom probe tomography I. Microstructural changes as a function of ageing temperature, Acta Mater. 101 (2015) 136–148.
[8] W. Tu, J. Tang, Y. ZHANG, L. Ye, S. Liu, J. Lu, X. Zhan, et al., Effect of Sn and Cu addition on the precipitation and hardening behavior of Al–1.0Mg–0.6Si alloy, Mat. Sci. Eng. A 770 (2020) 138515.
[9] L. Ding, Z. Jia, J.-F. Nie, Y. Weng, L. Cao, H. Chen, X. Wu, et al., The structural and compositional evolution of precipitates in Al–Mg–Si–Cu alloy, Acta Mater. 145 (2018) 437–450.
[10] O. Engler, C.D. Marioara, Y. Aruga, M. Kozuka, O.R. Myhr, Effect of natural ageing or pre-ageing on the evolution of precipitate structure and strength during age hardening of Al–Mg–Si alloy AA 6016, Mat. Sci. Eng. A 759 (2019) 520–529.
[11] G.H. Tao, C.H. Liu, J.H. Chen, Y.X. Lai, P.P. Ma, L.M. Liu, The influence of Mg/Si ratio on the negative natural aging effect in Al–Mg–Si–Cu alloys, Mat. Sci. Eng. A 642 (2015) 241–248.
[12] Yasuo Takaki, Tetsuya Masuda, Equo Kobayashi, Tatsuo Sato, Effects of natural aging on bake hardening behavior of Al–Mg–Si alloys with multi-step aging process, Mater. Trans. 55 (2014) 1257–1265.
[13] S. Pogatscher, H. Antrekowitsch, H. Leitner, D. Pöschmann, Z.L. Zhang, P.J. Uggowitzer, Influence of interrupted quenching on artificial aging of Al–Mg–Si alloys, Acta Mater. 60 (2012) 4496–4505.
[14] Z. Yang, Z. Liang, D. Leyvraz, J. Banhart, Effect of pre-aging on natural secondary ageing and paint bake hardening in Al–Mg–Si alloys, Materialia (2019) 100413.
[15] L. Ding, Y. Weng, S. Wu, R.E. Sanders, Z. Jia, Q. Liu, Influence of interrupted quenching and pre-aging on the bake hardening of Al–Mg–Si Alloy, Mat. Sci. Eng. A 651 (2016) 991–998.
[16] X. Xuehong, Y. Deng, C. Shuiqing, G. Xiaobin, Effect of interrupted ageing treatment on the mechanical properties and intergranular corrosion behavior of Al–Mg–Si alloys, J. Mater. Res. Technol. 9 (2020) 230–241.
[17] C.L. Liu, Q. Du, N.C. Parson, W.J. Poole, The interaction between Mn and Fe on the precipitation of Mn/Fe dispersoids in Al–Mg–Si–Mn–Fe alloys, Scr. Mater. 152 (2018) 59–63.
[18] N.C.W. Kuijpers, F.J. Vermolen, C. Vuik, P.T.G. Koenis, K.E. Nilsen, S. van der Zwaag, The dependence of the $\beta$-AlFeSi to $\alpha$-Al(FeMn)Si transformation kinetics in Al–Mg–Si alloys on the alloying elements, Mat. Sci. Eng. A 394 (2005) 9–19.
[19] L. Lodgaardm, N. Ryum, Precipitation of dispersoids containing Mn and/or Cr in Al–Mg–Si alloys, Mat. Sci. Eng. A 283 (2000) 144–152.
[20] X. Qian, N. Parson, X.-G. Chen, Effects of Mn content on recrystallization resistance of AA6082 aluminum alloys during post-deformation annealing, J. Mater. Sci. Technol. (2020).
[21] C. Li, K. Liu, X.-G. Chen, Improvement of elevated-temperature strength and recrystallization resistance via Mn-containing dispersoid strengthening in Al–Mg–Si 6082 alloys, J. Mater. Sci. Technol. 39 (2020) 135–143.
[22] M. Kenyon, J. Robson, J. Fellowes, Z. Liang, Effect of dispersoids on the microstructure evolution in Al–Mg–Si alloys, Adv. Eng. Mater. 6 (2018) 1800494.
[23] K.E. Knipling, D.C. Dunand, D.N. Seidman, Criteria for developing castable, creep-resistant aluminum-based alloys – a review, MEKU 97 (2006) 246–265.
[24] N.Q. Vo, D.C. Dunand, D.N. Seidman, Role of silicon in the precipitation kinetics of dilute Al–Sc–Er–Zr alloys, Mat. Sci. Eng. A 677 (2016) 485–495.
[25] C. Yang, P. Zhang, D. Shao, R.H. Wang, L.F. Cao, J.Y. Zhang, G. Liu, et al., The influence of Sc solute partitioning on the microalloying effect and mechanical properties of Al–Cu alloys with minor Sc addition, Acta Mater. 119 (2016) 68–79.
[26] H. Hu, M. Zhao, X. Wu, Z. Jia, R. Wang, W. Li, Q. Liu, The structural stability, mechanical properties and stacking fault energy of Al 3 Zr precipitates in Al–Cu–Zr alloys, J. Alloys Compd. 681 (2016) 96–108.
[27] S. Kumar Makineni, S. Sugathan, S. Meher, R. Banerjee, S. Bhattacharya, S. Kumar, K. Chattopadhyay, Enhancing elevated temperature strength of copper containing aluminium alloys by forming L12 Al3Zr precipitates and nucleating $\theta''$ precipitates on them, Sci. Rep. 7 (2017) 11154.
[28] H. Zhao, Y. Chen, B. Gault, S.K. Makineni, D. Ponge, D. Raabe, (Al, Zn)3Zr dispersoids assisted $\eta$’ precipitation in a model Al–Zn–Mg–Cu–Zr alloy, Materialia 10 (2020) 100641.
[29] A.B. Spierings, K. Dawson, T. Heeling, P.J. Uggowitzer, R. Schäublin, F. Palm, K. Wegener, Microstructural features of Sc- and Zr-modified Al–Mg alloys processed by selective laser melting, Mater. Des. 115 (2017) 52–63.
[30] A.B. Spierings, K. Dawson, P. Dumitraschkewitz, S. Pogatscher, K. Wegener, Microstructure characterization of SLM-processed Al–Mg–Sc–Zr alloy in the heat treated and HIPed condition, Addit. Manuf. 20 (2018) 173–181.
[31] S. Griffiths, M.D. Rossell, J. Croteau, N.Q. Vo, D.C. Dunand, C. Leinenbach, Effect of laser rescanning on the grain microstructure of a selective laser melted Al–Mg–Zr alloy, Mater. Charact. 143 (2018) 34–42.
[32] K.S. Kumar, S.A. Borwn, J.R. Pickens, Microstructural evolution during aging of an Al–Cu–Li–Ag–Mg–Zr alloy, Acta Mater. 44 (1996).
[33] S. Liu, W. Liu, Y. ZHANG, X. Zhang, Y. Deng, Effect of microstructure on the quench sensitivity of AlZnMgCu alloys, J. Alloys Compd. 507 (2010) 53–61.
[34] C. Shi, X.-G. Chen, Effect of Zr addition on hot deformation behavior and microstructural evolution of AA7150 aluminum alloy, Mater. Sci. Eng.: A 596 (2014) 183–193.
[35] S. Babaniaris, M. Ramajayam, L. Jiang, T. Langan, T. Dorin, Tailored precipitation route for the effective utilisation of Sc and Zr in an Al–Mg–Si alloy, Materialia 10 (2020) 100656.
[36] J. Fu, Z. Yang, Y. Deng, Y. Wu, J. Lu, Influence of Zr addition on precipitation evolution and performance of Al–Mg–Si alloy conductor, Mat. Charact. 159 (2020) 110021.
[37] R. Li, M. Wang, Z. Li, P. Cao, T. Yuan, H. Zhu, Developing a high-strength Al–Mg–Si–Sc–Zr alloy for selective laser melting: crack-inhibiting and multiple strengthening mechanisms, Acta Mater. (2020).

[38] T. Dorin, M. Ramajayam, S. Babaniaris, T.J. Langan, Micro-segregation and precipitates in as-solidified Al–Sc–Zr–(Mg)–(Si)–(Cu) alloys, Mat. Charact. 154 (2019) 353–362.
[39] Y. Liu, M. Tang, C. Wu, J. Wang, X. Su, Progress on phase equilibria of the Al Si Zr system at 700 and 900°C, J. Alloys Compd. 693 (2017) 357–365.
[40] K.E. Knipling, D.C. Dunand, D.N. Seidman, Precipitation evolution in Al–Zr and Al–Zr–Ti alloys during aging at 450–600°C, Acta Mater. 56 (2008) 1182–1195.
[41] L. Litynska, D. Abou-Ras, G. Kostorz, J. Dutkiewicz, TEM and HREM study of Al3Zr precipitates in an Al–Mg–Si–Zr alloy, J. Microsc. 223 (2006) 182–184.
[42] T. Gao, A. Ceguerra, A. Breen, X. Liu, Y. Wu, S. Ringer, Precipitation behaviors of cubic and tetragonal Zr–rich phase in Al–(Si–)Zr alloys, J. Alloys Compd. 674 (2016) 125–130.
[43] Y. Meng, J. Cui, Z. Zhao, L. He, Effect of Zr on microstructures and mechanical properties of an AlMgSiCuCr alloy prepared by low frequency electromagnetic casting, Mater. Charact. 92 (2014) 138–148.
[44] Y. Birol, Optimization of homogenization for a low alloyed AlMgSi alloy, Mat. Charact. 80 (2013) 69–75.
[45] J.H. Li, A. Wimmer, G. Dehm, P. Schumacher, Intermetallic phase selection during homogenization for AA6082 alloy, Philos. Mag. 94 (2014) 830–846.
[46] L. Yan, Y.-A. Zhang, X.-W. Li, Z.-H. Li, F. Wang, H.-W. Liu, B.-Q. Xiong, Microstructural evolution of Al–0.66Mg–0.85Si alloy during homogenization, Trans. Nonferrous Metals Soc. China 24 (2014) 939–945.
[47] M. Rahimian, S. Amirkhanlou, P. Blake, S. Ji, Nanoscale Zr-containing precipitates; a solution for significant improvement of high-temperature strength in Al–Si–Cu–Mg alloys, Mat. Sci. Eng. A 721 (2018) 328–338.
[48] Y. Birol, Effect of Cr and Zr on the grain structure of extruded EN AW 6082 alloy, Met. Mater. Int. 20 (2014) 727–732.
[49] Normenausschuss für Nichteisenmetalle, Aluminium und Aluminiumlegierungen – Chemische Zusammensetzung und Form von Halbzeug(DIN EN 573-3) 2013.
[50] F. Schmid, L. Stemper, T. Ebner, S. PogatscherGDMB, Industry-oriented sample preparation of 6xxx and 5xxx aluminum alloys in laboratory scale, EMC 2019: Optimum Utilization of Resources and Recycling for a Sustainable Solution, 2019.
[51] C.W. Bale, P. Chartrand, S.A. Degterov, G. Eriksson, K. Hack, R.B. Mahfoud, J. Melancon, et al., FactSage thermochemical software and databases, Calphad 26 (2002) 189–228.
[52] C.W. Bale, E. Bélisle, P. Chartrand, S.A. Decterov, G. Eriksson, K. Hack, I.-H. Jung, et al., FactSage thermochemical software and databases — recent developments, Calphad 33 (2009) 295–311.
[53] J. Friel, S. Wright, S. Sitzman, ASTM grain size by EBSD – a new standard, Microsc. Microanal. 17 (2011) 838–839.
[54] J. Grasserbauer, I. Weißensteiner, G. Falkinger, S. Mitsche, P.J. Uggowitzer, S. Pogatscher, Evolution of microstructure and texture in laboratory- and industrial-scaled production of automotive Al-sheets, Materials 13 (2020).
[55] F. Bachmann, R. Hielscher, H. Schaeben, Grain detection from 2d and 3d EBSD data–specification of the MTEX algorithm, Ultramicroscopy 111 (2011) 1720–1733.
[56] R. Hielscher, C.B. Silbermann, E. Schmidl, J. Ihlemann, Denoising of crystal orientation maps, J. Appl. Crystallogr. 52 (2019) 984–996.
[57] M.H. Larsen, J.C. Walmsley, O. Lunder, R.H. Mathiesen, K. Nisancioglu, Intergranular corrosion of copper-containing AA6xxx AlMgSi aluminum alloys, J. Electrochem. Soc. 155 (2008) C550.
[58] P.H. Ninive, A. Strandlie, S. Gulbrandsen-Dahl, W. Lefebvre, C.D. Marioara, S.J. Andersen, J. Friis, et al., Detailed atomistic insight into the $\beta''$ phase in Al–Mg–Si alloys, Acta Mater. 69 (2014) 126–134.
[59] J.A. Österreicher, M. Kumar, A. Schiffl, S. Schwarz, G.R. Bourret, Secondary precipitation during homogenization of Al–Mg–Si alloys, Mat. Sci. Eng. A 687 (2017) 175–180.
[60] C. Wolverton, Crystal structure and stability of complex precipitate phases in Al–Cu–Mg–(Si) and Al–Zn–Mg alloys, Acta Mater. 49 (2001) 3129–3142.
[61] C. Cayron, P.A. Buffat, Transmission electron microscopy study of the $\beta'$ phase (Al–Mg–Si alloys) and QC phase (Al–Cu–Mg–Si alloys) ordering mechanism and crystallographic structure, Acta Mater. 48 (2000) 2639–2653.
[62] R.H. Kemsies, B. Milkereit, S. Wenner, R. Holmestad, O. Kessler, In situ DSC investigation into the kinetics and microstructure of dispersoid formation in Al-Mn-Fe-Si(-Mg) alloys, Mater. Des. 146 (2018) 96–107.
[63] A.V. Mikhaylovskaya, A.G. Mochugovskiy, V.S. Levchenko, N.Y. Tabachkova, W. Mufalo, V.K. Portnoy, Precipitation behavior of L12 Al3Zr phase in Al-Mg-Zr alloy, Mat. Charact. 139 (2018) 30–37.
[64] D. Tsivoulas, J.D. Robson, C. Sigli, P.B. Prangnell, Interactions between zirconium and manganese dispersoid-forming elements on their combined addition in Al–Cu–Li alloys, Acta Mater. 60 (2012) 5245–5259.
[65] G. Gottstein, Physikalische Grundlagen der Materialkunde, 3rd ed., Springer-Verlag, Berlin, Heidelberg, 2007.
[66] A. Kelly, R.B. Nicholson, Precipitation hardening, Progr. Mater. Sci. (1964) 149–391.
[67] G.P.M. Leyson, L.G. Hector, W.A. Curtin, Solute strengthening from first principles and application to aluminum alloys, Acta Mater. 60 (2012) 3873–3884.
[68] J. Banhart, C.S.T. Chang, Z. Liang, N. Wanderka, M.D.H. Lay, A.J. Hill, Natural aging in Al–Mg–Si Alloys – a process of unexpected complexity, Adv. Eng. Mater. 12 (2010) 559–571.
[69] Q. Dong, A. Howells, M.F. Gallerneault, V. Fallah, Precipitation-induced mitigation of recrystallization in ultra-thin, cold-rolled AlScZrMn(Mg) sheets at brazing temperatures: the critical effect of alloy composition and thermal processing route, Acta Mater. 186 (2020) 308–323.
[70] E. Nes, N. Ryum, O. Hunderi, On the Zener drag, Acta Metall. 33 (1985) 11–22.
[71] X. Wang, J. Qin, H. Nagaumi, R. Wu, Q. Li, The effect of $\alpha$-Al(MnCr)Si dispersoids on activation energy and workability of Al–Mg–Si–Cu alloys during hot deformation, Adv. Mater. Sci. Eng. 2020 (2020) 1–12.
[72] J.A. Österreicher, F. Grabner, A. Schiffl, S. Schwarz, G.R. Bourret, Information depth in backscattered electron microscopy of nanoparticles within a solid matrix, Mat. Charact. 138 (2018) 145–153.
[73] H.J. McQueen, W. Blum, Dynamic recovery sufficient mechanism in the hot deformation of Al (99.99), Mat. Sci. Eng. A 290 (2000) 95–107.
[74] T.J. Ginter, A.M. Farghalli, The stress dependence of the subgrain size in aluminium, J. Mater. Sci. 17 (1982) 2007–2012.
[75] B. Gruber, F. Grabner, W. Fragner, A. Schökel, F. Spieckermann, P.J. Uggowitzer, S. Pogatscher, Ageing behaviour of Al-Mg-Si alloys after cryogenic and room temperature deformation, Materials 13 (2020).
[76] T. Sun, X. Wu, M. Zhao, Z. Jia, R. Wang, W. Li, Q. Liu, Segregation and mechanical properties of Si, Fe and Ti on the Al/Al 2.5 X 0.5 Zr (X = Cu, Zn, Ag) coherent interfaces, Comput. Mater. Sci. 141 (2018) 325–340.
[77] P. Dumitraschkewitz, S.S.A. Gerstl, L.T. Stephenson, P.J. Uggowitzer, S. Pogatscher, Clustering in age-hardenable aluminum alloys, Adv. Eng. Mater. 20 (2018) 1800255.
[78] S. Pogatscher, H. Antrekowitsch, H. Leitner, T. Ebner, P.J. Uggowitzer, Mechanisms controlling the artificial aging of Al–Mg–Si Alloys, Acta Mater. 59 (2011) 3352–3363.